



Effect of annealing on microstructure and properties of AlCoCuFeTi high-entropy alloy fabricated by arc melting

Xuanjiang Lai ^{a,b}, Yaojia Ren ^a, Qingge Wang ^a, Shaohua Xing ^b, Cheng Xu ^b, Jian Hou ^{b,**}, Ian Baker ^c, Hong Wu ^{a,*}

^a State Key Laboratory of Powder Metallurgy, Central South University, Changsha, 410083, China

^b National Key Laboratory of Marine Corrosion and Protection, Luoyang Ship Material Research Institute, Qingdao, 266237, China

^c Thayer School of Engineering, Dartmouth College, Hanover, NH, 03755-8000, USA

ARTICLE INFO

Keywords:

High-entropy alloys
Annealing heat treatment
Microstructure
Nanomechanical behaviors
Wear resistance
Corrosion resistance

ABSTRACT

An AlCoCuFeTi high-entropy alloy with excellent wear resistance and high hardness was successfully produced by arc melting. The effects of annealing on the microstructure, nanomechanical behaviors, tribological properties, and corrosion resistance were systematically investigated. The results showed that the AlCoCuFeTi consisted of a Co-enriched L2₁ phase, a Cu-enriched FCC phase, and a (Fe, Ti)-enriched Laves phase. Annealing promoted the formation of FCC and Laves phases but decreased the volume fraction of the L2₁ phase. The high hardness of AlCoCuFeTi is attributed to the formation of L2₁ and Laves phases. The highest hardness (14.1 ± 1.3 GPa) and reduced Young's modulus (256 ± 11 GPa) were achieved in the 1100 °C annealed and 900 °C annealed specimens, respectively. All specimens exhibited excellent wear resistance compared to typical HEAs due to the mild-oxidative wear mechanism. The 1100 °C annealed specimen possessed the highest elastic strain to failure (H/E_r) and yield pressure (H³/E_r²), corresponding to its best-measured wear resistance. The segregation of Cu led to galvanic corrosion during the polarization tests, and the area ratio of cathode to anode (A_c/A_a) determined the corrosion rate. The 1100 °C annealed specimen exhibited good corrosion resistance due to its low A_c/A_a value.

1. Introduction

As emerging metallic materials, high-entropy alloys (HEAs) can exhibit excellent mechanical properties, good tribological properties, high hardness, outstanding corrosion resistance, and remarkable oxidation resistance, making them strong candidates for applications in both the aerospace and automobile industries and other engineering fields [1–10]. Unlike traditional alloying strategies based on one or two principal elements, HEAs typically consist of at least five principal elements with greater than 5 at. % of each element [11–13]. The high mixing entropy and minor atomic size differences in transition-metal HEAs can lead to the formation of simple solid-solution phases such as face-centered cubic (FCC), body-centered cubic (BCC), or hexagonal close-packed (HCP) structures [14–16]. It is well known that FCC-structured HEAs generally exhibit outstanding ductility but low strength, whereas BCC-structured HEAs exhibit good strength but low ductility. Thus, an increasing number of researchers have focused on

dual-phase structures HEAs due to the combination of strength and plasticity. AlCoCuFeNi is an outstanding dual-phase HEA whose microstructure and mechanical properties have been widely studied [17–21]. However, the low hardness and poor wear resistance of AlCoCuFeNi limits its use. As an alloying element in HEAs, titanium (Ti) has excellent potential to improve the hardness and tribological properties by facilitating the formation of a Laves phase [22]. For example, Li et al. [23] reported that the wear rate of Ti_xCrFeCoNiCu HEAs decreased from $2.26 \times 10^{-4} \text{ mm}^3 \text{ N}^{-1} \text{ m}^{-1}$ to $9.92 \times 10^{-7} \text{ mm}^3 \text{ N}^{-1} \text{ m}^{-1}$ when the Ti content was increased from x = 0 to x = 0.8. This improvement was attributed to the formation of the Laves phase and the lattice distortion. Similar results have been found by Zhao et al. [24], the volume fraction of Laves phase increased in CoCrFeNiTi_x HEAs as the Ti content increased. The addition of 16.7 at.% Ti to CuCoFeNi has been shown to increase the hardness from 157 HV to 462 HV [25]. Hence, the Ni in AlCoCuFeNi was replaced by Ti with the aim of improving the hardness and wear resistance, thus broadening its engineering applications. In

* Corresponding author.

** Corresponding author.

E-mail addresses: houjian@sunrui.net (J. Hou), wuhong927@126.com (H. Wu).

addition to hardness and tribological properties, corrosion resistance is also critical for HEAs. While the electrode potential of Ti is lower than that of Ni, Ti-containing HEAs have excellent corrosion resistance in many aqueous environments because of their low passivation potential and broad passivation zone [26,27]. Zhao et al. [27] reported that the $\text{Al}_{2-x}\text{CoCrFeNiTi}_x$ alloys had a higher corrosion resistance than $\text{Al}_2\text{CoCrFeNi}$ alloy in 3.5 wt% NaCl solution due to the formation of passive films. Zhuang et al. [28] reported that the $\text{Al}_{0.3}\text{CoCrFeNiTi}_x$ HEAs exhibit improved corrosion resistance to Cl^- when the Ti content increases from $x = 0$ to $x = 0.5$.

In addition to altering the elemental composition, heat treatment is also an efficient method to obtain HEAs with excellent properties. Several studies have discovered that annealed HEAs have higher hardness and better wear and corrosion resistance than as-cast HEAs [29–31]. For example, $\text{AlCoCrFeNiTi}_{0.5}$ annealed at 800 °C for 2 h showed a higher microhardness (~680 HV for FCC and ~770 HV for BCC) compared with the as-cast alloy (~600 HV for FCC and ~750 HV for BCC) [32]. Chen et al. [33] observed that the nanohardness of AlCoCrFeNi was improved by annealing due to the precipitation of FCC and σ phases. Zhang et al. [34] reported that the microhardness and wear resistance of laser-clad $\text{AlCoCrFeNiTi}_{0.5}$ was increased by annealing at 900 °C. Kong et al. [35] found that the tribological properties of as-cast $\text{AlCoCrFeNiTi}_{0.5}$ HEAs after surface remelting were improved with subsequent annealing. Furthermore, Zhao et al. [36] found the $\text{Al}_{0.6}\text{CoFeNiCr}_{0.4}$ aged at 550 °C exhibited better corrosion resistance than the as-cast alloy. Similarly, Liaw et al. [37] reported the corrosion resistance of AlCoCrFeNi was improved after heat treatment at 1250 °C because of the reduction of elemental segregation.

Thus, in this study, we designed an AlCoCuFeTi HEA with good wear resistance and high hardness based on the AlCoCuFeNi HEA. The effect of different annealing temperatures on the phase present, microstructural evolution, nanomechanical behaviors, tribological properties, and corrosion resistance of equiautomic AlCoCuFeTi are investigated and discussed.

2. Materials and methods

An AlCoCuFeTi ingot was fabricated by arc melting high purity (>99.5 wt%) Al, Co, Cu, Fe, and Ti elemental pieces under a high-purity argon atmosphere on a water-cooled copper hearth. The resulting button was melted at least five times to ensure all elements were mixed uniformly. The AlCoCuFeTi ingot was sectioned into specimens using wire cutting and annealed at either 900 °C or 1100 °C for 10 h, hereafter referred to as-cast, A900 and A1100 specimens, respectively.

Thermal analysis was performed on a differential scanning calorimeter (DSC, Q2000) under an argon atmosphere at a heating rate of 10 °C/min. The phase fraction of the AlCoCuFeTi HEA at different temperatures was calculated using PANDAT software. The phase present was determined using an X-ray diffractometer (XRD, PIGAKV D/Max 2550) with Cu-K α radiation. The scanning angle (2θ) ranged from 30° to 90° at a step of 0.02°. The specimens were mechanically ground and polished through standard methods before the microstructure was observed. The microstructure was examined using a scanning electron microscope (SEM, Quanta FEG250) equipped with an electron back-scatter diffraction (EBSD) detector and an X-ray energy dispersive spectroscopy (EDS). The elemental distribution was characterized using an electron probe microanalyzer (EPMA, JXA-8230, Japan). A higher-resolution microstructure was observed using a transmission electron microscope (TEM, FEI Talos F200X) equipped with an EDS detector. The TEM specimens were mechanically ground into slices of about 50 μm thickness and punched into disks with a diameter of 3 mm before electropolishing.

Berkovich-tip nanoindentation (NanoTest Vantage, United Kingdom) was used to characterize the nanohardness and modulus of the different phases. The maximum load was set to 30 mN with a hold time of 15 s, loading and unloading rates of 1 mN/s. Dry sliding wear tests were

performed at room temperature with a ball-on-disk tribometer (HT-1000, China) using a 4 mm Si_3N_4 ceramic ball with an applied load of 10 N. The sliding velocity and sliding time were 117 mm/s and 30 min, respectively. The tests were repeated three times. The worn surfaces and element distributions were observed using the SEM, and the worn surface profile was examined using a 3D optical profilometer (Keyence VHX-5000, Japan).

The polarization tests were performed on an electrochemical workstation (CHI660D, China) with a normal three-electrode system. The specimens were tested in a 3.5 wt% NaCl solution at room temperature. The open circuit potential (OCP) was measured to reach a stable potential for 3600 s. The potentiodynamic-polarization curves were collected at a scanning rate of 1 mV/s with a potential range from -1.5 V to 1.0 V. The corroded surfaces were examined using the SEM.

3. Results

3.1. Phase identification

Fig. 1(a) shows DSC curves of as-cast AlCoCuFeTi from 400 to 1100 °C. The exothermic peak is present at 1034 °C, while an endothermic peak occurred at 1052 °C. These phenomena are associated with the occurrence of a phase transformation or the melting of a phase during heating. **Fig. 1(b)** presents the phase equilibria calculations for AlCoCuFeTi . The Cu-rich FCC phase disappears and the liquid phase occurs at 1035 °C. Thus, the endothermic peak at 1052 °C in **Fig. 1(a)** is due to the melting of the Cu-rich FCC phase.

Fig. 2(a) shows the XRD pattern from as-cast, A900, and A1100 specimens. The XRD results indicate that the specimens consist of three phases: an ordered L_{21} phase (AlCo_2Ti , lattice parameter: $a = 0.5847 \text{ nm}$), an FCC phase (Cu, lattice parameter: $a = 0.3615 \text{ nm}$), and a Laves phase (Fe_2Ti , lattice parameter: $a = b = 0.4785 \text{ nm}$, $c = 0.7799 \text{ nm}$). The Laves phase is an intermetallic compound often observed in the AlCoCrFeNiTi system [27]. No new phases are observed after annealing, which is consistent with the DSC results. **Fig. 2 (b)** shows the phase volume fractions of L_{21} , FCC, and Laves phases in as-cast and annealed specimens. With increasing annealing temperature, the volume fractions of FCC and Laves phases increase while that of L_{21} decreases. The as-cast specimen is mainly composed of L_{21} phase (90.1%). A small amount of Laves phase (3.4%) and FCC phase (6.5%) are also detected. For the A900 specimen, the volume fraction of L_{21} phase slightly decreases to 84.2%, while the volume fraction of Laves and FCC phases increase to 5.4% and 10.4%. Compared with the as-cast specimen, the L_{21} phase volume fraction in the A1100 specimen is significantly less at 70.4%, whereas the Laves phase volume fraction has increased to 16.4%.

3.2. Microstructure and elemental distribution analysis

Backscattered electron (BSE) images of three specimens at different magnifications are shown in **Fig. 3**. The typical cast microstructure, which consists of dendrites (DR) and interdendritic regions (ID), is observed in the as-cast specimen, as shown in **Fig. 3(a₁)**. After annealing at 900 °C for 10 h, the cast dendritic microstructure feature weakened, which can be seen in **Fig. (b₁)**. However, the cast dendritic microstructure disappears in the A1100 specimen and is replaced by a circular island structure, see **Fig. 3(c₁)**. **Fig. 3(a₂-c₂)** clearly show that all specimens are composed of three phases: a majority dark matrix phase, a bright phase, and a gray phase. After the specimen is annealed at 900 °C and 1100 °C, the gray phase experiences growth, and in the A1100 specimen, the gray phase has clearly coarsened compared with both the as-cast and A900 specimens. **Fig. 4** shows BSE images and Al, Co, Cu, Fe, and Ti elemental distribution maps for as-cast, A900, and A1100 specimens. The distribution of elements is heterogeneous. Based on the element distribution maps and XRD results, the dark phase is enriched in Al, Co, and Ti and is L_{21} , while the bright phase is enriched in Cu and is FCC. In addition, the gray phase is enriched in Fe and Ti and is the Laves

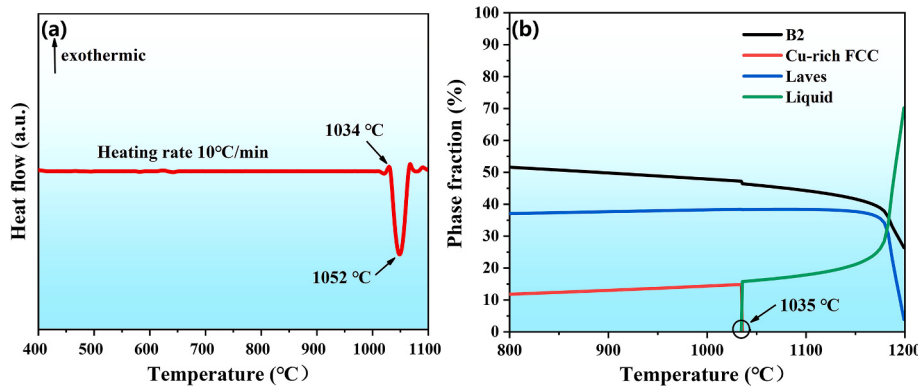


Fig. 1. (a) DSC curve, and (b) calculated equilibrium phase fractions versus temperature for as-cast AlCoCuFeTi.

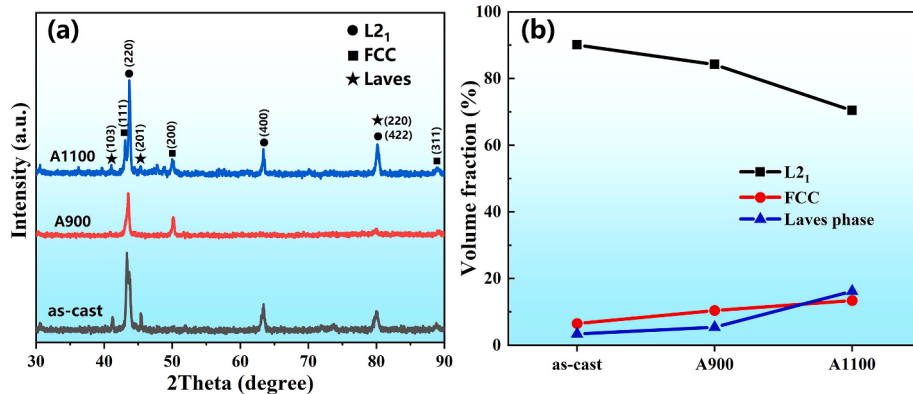


Fig. 2. (a) XRD patterns (b) volume fractions of the phases in as-cast, A900, and A1100 AlCoCuFeTi specimens.

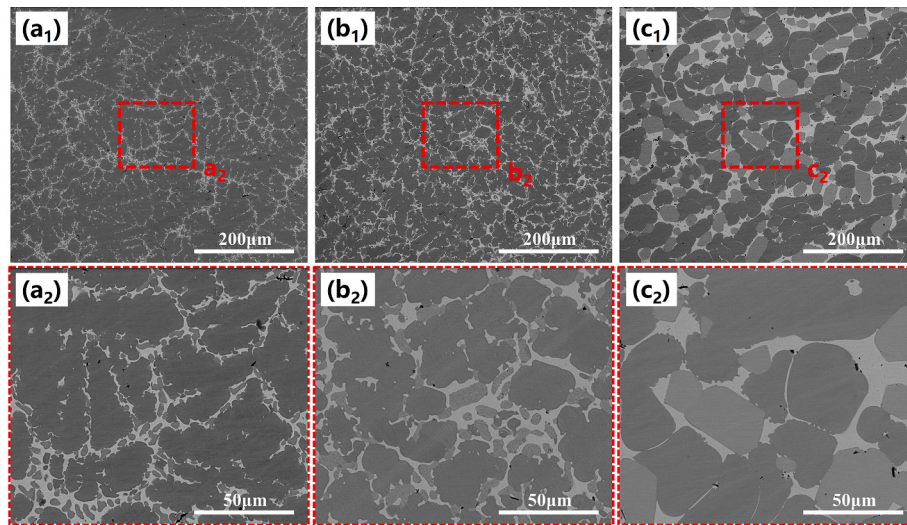


Fig. 3. BSE images of (a1) as-cast, (b1) A900, and (c1) A1100 specimens, (a2-c2) are corresponding magnified images of the red boxes in (a1-c1).

phase with a C14 structure [38,39].

To further identify the structure of AlCoCuFeTi HEA, a TEM analysis was conducted. Fig. 5 shows the bright field-TEM (BF-TEM) images and corresponding selected area electron diffraction (SAED) patterns of different phases in AlCoCuFeTi HEA. The SAED patterns reveal that the AlCoCuFeTi HEA is composed of BCC, FCC, and Laves phases. Note that some superlattice spots (marked with red circles) can be observed in Fig. 5(c) at [100] zone axis, indicating that the BCC phase is an ordered L2₁ phase. In addition, some precipitates are observed in Fig. 5(a) and

(b). Fig. 6(a) shows the detail of precipitates in the L2₁ phase. The shape of the precipitates is rectangular or rhombic and with a size of ~20 nm. Fig. 6(b) shows the high-resolution TEM (HRTEM) images of the precipitates. The corresponding Fourier transformation (FFT) patterns are shown in Fig. 6(c). The superlattice spots (marked with red circles) indicate that the precipitates have an ordered L2₁ structure. The STEM-EDS mappings (Fig. 6(d)) show that the L2₁ precipitates are enriched in Cu. The same Cu-rich L2₁ phase was also observed in AlCuTiVCr HEA [40] and titanium alloy [41].

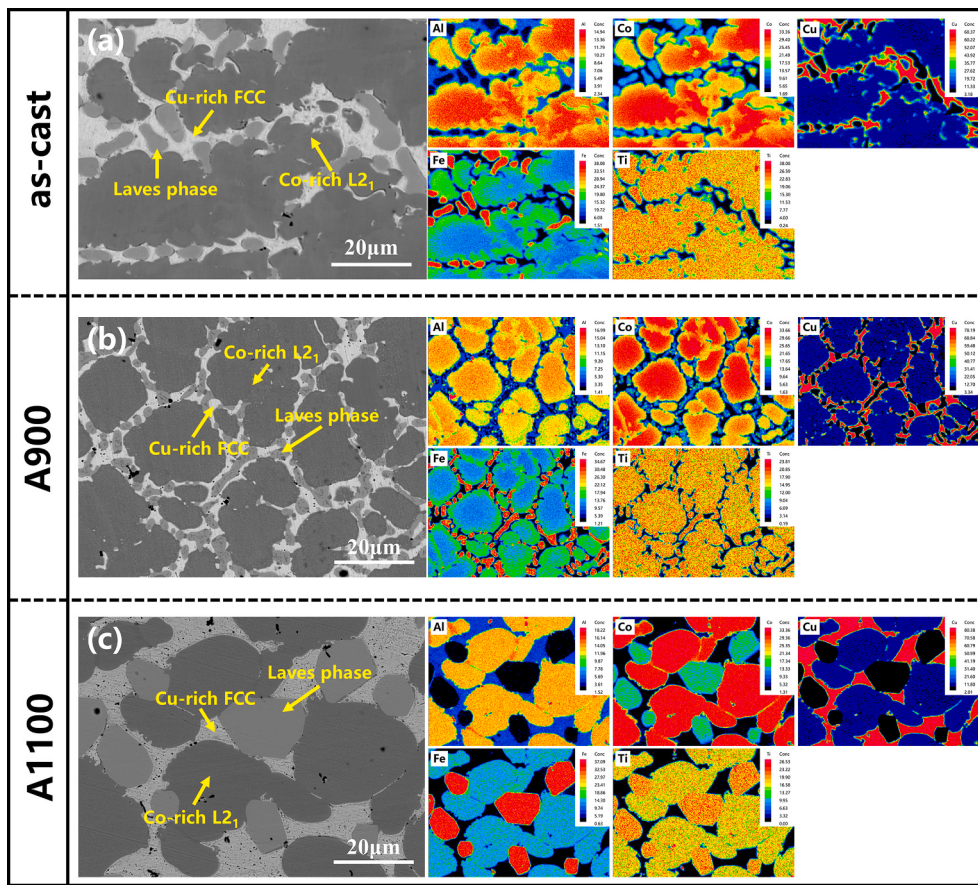


Fig. 4. BSE images and EPMA maps of AlCoCuFeTi HEA: (a) as-cast, (b) A900, and (c) A1100 specimens.

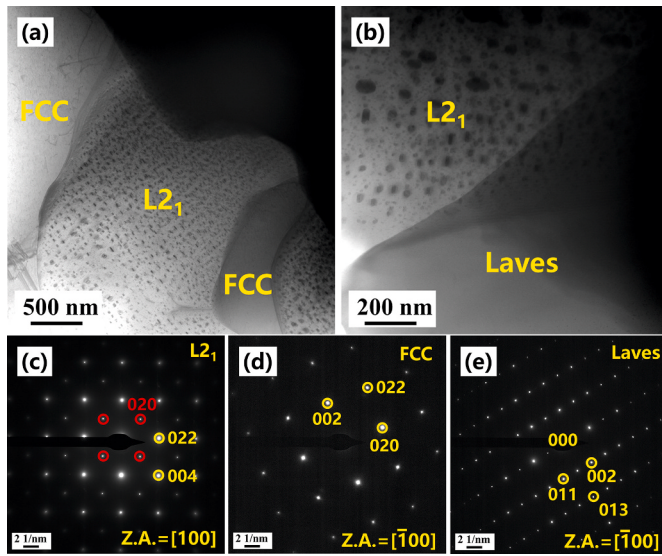


Fig. 5. (a)–(b) BF-TEM images of L₂₁, FCC, and Laves phases in A900 specimen, (c)–(e) corresponding SAED patterns.

3.3. Nanomechanical behaviors

Fig. 7(a) shows the average nanohardness and reduced Young's modulus of the as-cast and annealed AlCoCuFeTi alloys. The average nanohardness values of as-cast, A900, and A1100 specimens are 12.3 ± 1.8 GPa, 11.6 ± 1.2 GPa, and 14.1 ± 1.3 GPa, respectively, while the reduced Young's modulus of as-cast, A900, and A1100 specimens are

213 ± 27 GPa, 256 ± 11 GPa, and 234 ± 14 GPa, respectively. The A900 specimen exhibits the highest reduced Young's modulus but the lowest hardness. Further, the nanohardness and reduced Young's modulus of each phase in the A1100 sample are measured, as shown in **Fig. 7(b)**. The nanohardness values of L₂₁, FCC, and Laves phase are 13.3 ± 0.9 GPa, 4.2 ± 0.8 GPa, and 15.8 ± 0.5 GPa, respectively. **Fig. 7(c)** presents the Displacement-Load (D-L) curves of different phases in the A1100 specimen. From **Fig. 7(c)**, the maximum displacement value (~ 483 nm) is observed in FCC, while the minimum value (~ 152 nm) is observed in the Laves phase. In addition, the L₂₁ phase has a similar displacement value (~ 196 nm) to the Laves phase, which indicates its high hardness.

3.4. Tribological properties

Fig. 8(a) displays the friction coefficient of as-cast, A900, and A1100 specimens as a function of sliding time. The friction coefficient curves of all specimens are made up of the running-in stage and steady-state stage. The coefficient of friction (COF) fluctuates drastically in the running-in stage (about 450 s) due to the formation of small debris and increased contact area. After the running-in stage, the curves remain almost stable, and the average friction coefficients of as-cast, A900, and A1100 specimens are 0.47, 0.38, and 0.29, respectively. **Fig. 8(b)** presents the wear rates of as-cast, A900 and A1100 specimens, which are 2.04×10^{-5} mm³ N⁻¹ m⁻¹, 2.43×10^{-5} mm³ N⁻¹ m⁻¹ and 1.06×10^{-5} mm³ N⁻¹ m⁻¹, respectively. The results indicate that the A1100 specimen has the best wear resistance. **Table 1** compares the tribological properties of AlCoCuFeTi HEAs in this study with AlCoCuFeNi and other typical HEAs. The AlCoCuFeTi HEA exhibits the best tribological properties, which suggests that titanium plays a critical role in improving the wear resistance of HEAs.

To determine the tribological mechanisms, secondary electron (SE)

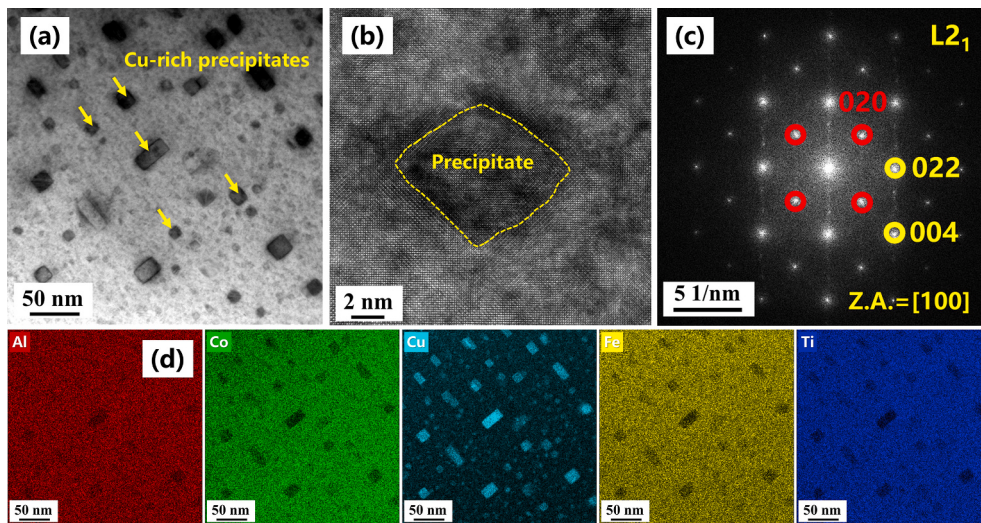


Fig. 6. TEM analysis of precipitates in L₂₁ phase: (a) BF-TEM image, (b) HRTEM image, (c) FFT patterns, (d) STEM-EDS mappings.

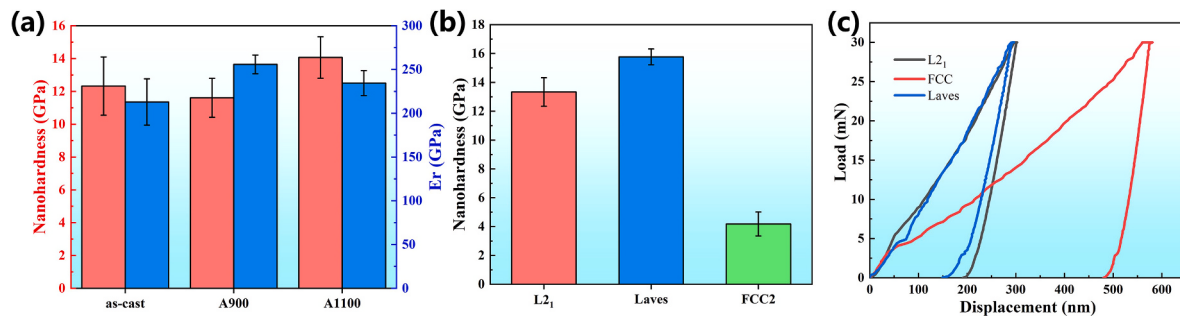


Fig. 7. (a) Average nanohardness and reduced Young's modulus of the as-cast and annealed AlCoCuFeTi HEAs; (b) nanohardness, and (c) Displacement-Load curves of L₂₁, FCC, and Laves phases in the A1100 specimen.

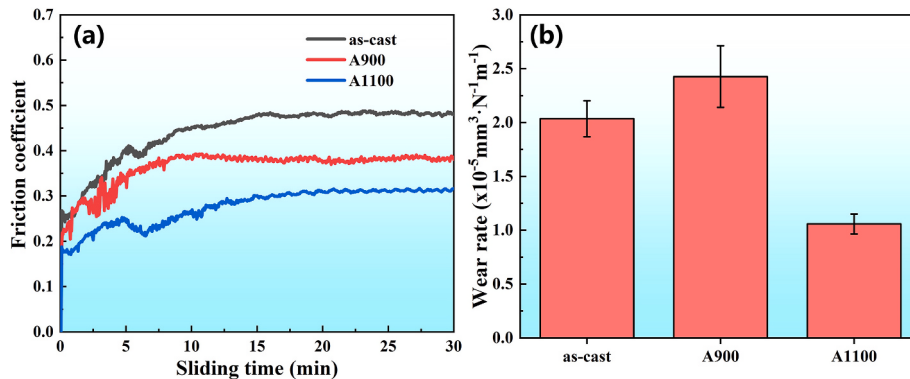


Fig. 8. (a) Friction coefficient versus sliding time, and (b) wear rate for as-cast and annealed AlCoCuFeTi HEAs.

images, 3D morphologies, and cross-sectional profiles of the worn surfaces for as-cast, A900, and A1100 specimens are examined. All specimens show shallow worn surface scratches, which means all specimens have good wear resistance, see Fig. 9(a–c). In addition, a glaze layer can be observed on the worn surfaces of all specimens. Table 2 shows EDS results from the worn surface, indicating that the glaze layers are made up of oxide. Thus, the wear mechanism of as-cast and annealed specimens is mild-oxidational wear [47,48]. The appearance of dense oxide film can be found in other studies on the tribological properties of HEAs [49–52]. Fig. 9(d–f) presents 3D morphologies of the worn surface in Fig. 9(a–c), and the corresponding cross-sectional profiles are shown in

Fig. 9(g–i). It can be seen from Fig. 9(g–i) that the minimum cross-sectional wear area occurred in the A1100 specimen ($1613 \mu\text{m}^2$). The cross-sectional wear areas of as-cast and A900 specimens are larger than that of A1100, indicating that A1100 has the best wear resistance, which is consistent with the wear rate results.

3.5. Corrosion resistance

Fig. 10 shows the potentiodynamic-polarization curves of as-cast and annealed AlCoCuFeTi HEAs tested in a 3.5 wt% NaCl solution. The corrosion potential (E_{corr}), corrosion current density (i_{corr}), pitting

Table 1

Comparison of the wear resistance of some typical HEAs at room temperature.

Alloy	Counterpart material	Wear rate ($10^{-5} \text{ mm}^3 \text{ N}^{-1} \text{ m}^{-1}$)	COF	Ref.
AlCoCuFeNi	Si ₃ N ₄	6.5	0.53	[42]
Al _{1.3} CoCuFeNi ₂	Si ₃ N ₄	120	0.62	[43]
Al _{0.5} CrCoCuFeNi	SKH-51	75	0.5	[44]
AlCrCoCuFeNi	SKH-51	~50	0.48	[44]
AlCoCrFeNi	Al ₂ O ₃	25	0.79	[45]
CoCrFeNi	Si ₃ N ₄	23	0.56	[46]
as-cast	Si ₃ N ₄	2.04	0.47	This work
A900	Si ₃ N ₄	2.43	0.38	This work
A1100	Si ₃ N ₄	1.06	0.29	This work

potential (E_{pit}), and passivation potential ($\Delta E_p = E_{\text{pit}} - E_{\text{corr}}$) can be extracted from the potentiodynamic-polarization curves, as shown in Table 3. The corrosion rate (CR) can be calculated from:

$$\text{CR} = K i_{\text{corr}} E_W \rho^{-1} \quad (1)$$

where CR represents the corrosion rate (mm/year), K is a constant (3.27×10^{-3}), i_{corr} is the corrosion current density ($\mu\text{A}/\text{cm}^2$), ρ is the alloy density (g/cm^3), and E_W is the equivalent weight. With the increase in annealing temperature, the E_{corr} and the i_{corr} decrease simultaneously. The A1100 specimen exhibits the lowest i_{corr} ($10.03 \mu\text{A}/\text{cm}^2$), indicating its best corrosion resistance. In contrast, the as-cast and A900 specimens have higher i_{corr} than the A1100 specimen, implying poor corrosion resistance. To further investigate the corrosion mechanism, SEM images and EDS mappings of corroded surfaces after the polarization test are examined, as shown in Fig. 11. It can be found that the corrosion mainly appears in the Cu-enriched FCC phase. In contrast, no significant corrosion occurs in L₂1 and Laves phases. This phenomenon is attributed to galvanic corrosion because of the potential difference between the Cu-rich FCC and other phases.

4. Discussion

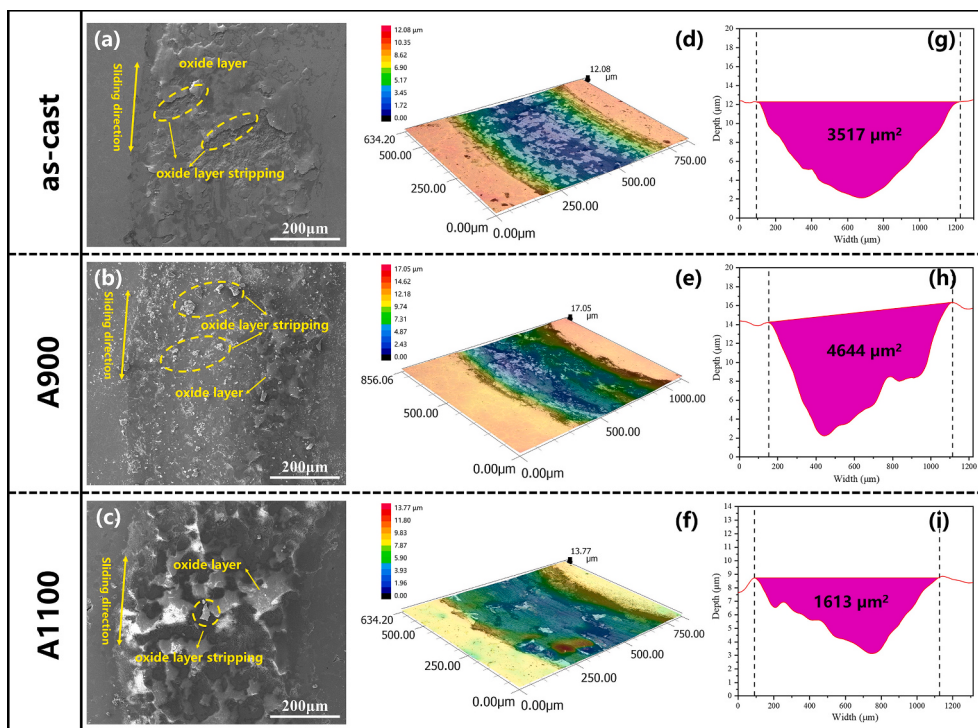
4.1. Microstructural evolution

Examination of the microstructure and elemental distribution show that Cu tends to segregate to the ID region. This is attributed to its positive mixing entropy with other alloying elements, as shown in Table 4. The mixing enthalpies of Cu with Co and Fe are +6 kJ/mol and +13 kJ/mol, respectively. It is difficult for Cu to react with other elements and form intermetallic compounds owing to the positive mixing enthalpies. However, the mixing enthalpies of Cu with Al and Ti are negative, indicating that a few Cu atoms can exist in the L₂1 phase, see Fig. 4. The mixing enthalpies of Al–Co, Al–Ti, Fe–Ti, and Co–Ti pairs possess low mixing enthalpies, which leads to Fe and Ti enrichment in Laves phase and Al, Co, and Ti enrichment in L₂1 phase. Sluggish diffusion is one of four core effects in HEAs, which can impede the formation of intermetallic compounds [53]. It is difficult for Ti and Cu atoms to diffuse at low temperatures on account of the larger atomic radius and sluggish diffusion. Thus, the as-cast specimen contains only a tiny amount of FCC and Laves phases. After annealing at 900 °C and 1100 °C, the volume fraction of FCC and Laves phases increased due to the high temperature during annealing, which increases the diffusion rate of Ti and Cu atoms. Simultaneously, the high temperature provided sufficient energy to coarsen the Laves phase.

Table 2

EDS results (at.%) from the worn surfaces of as-cast, A900, and A1100 specimens.

Specimen	Al	Ti	Fe	Co	Cu	O
as-cast	9.6 ± 0.6	13.3 ± 0.3	9.7 ± 0.4	9.0 ± 1.1	9.6 ± 1.2	48.8 ± 1.2
	0.6	0.3	0.4	1.1	0.2	3.5
A900	8.7 ± 1.3	12.4 ± 0.8	10.8 ± 0.4	10.3 ± 0.8	14.0 ± 0.2	43.8 ± 3.5
	0.1	0.4	0.8	0.8	0.2	3.5
A1100	6.4 ± 0.1	10.0 ± 0.4	9.0 ± 0.8	7.8 ± 0.6	7.2 ± 1.0	59.6 ± 2.5
	0.1	0.4	0.8	0.6	1.0	2.5

**Fig. 9.** (a–c) SE images; (d–f) 3D morphologies; and (g–i) cross-sectional profiles of wear tracks for as-cast, A900, and A1100 specimens.

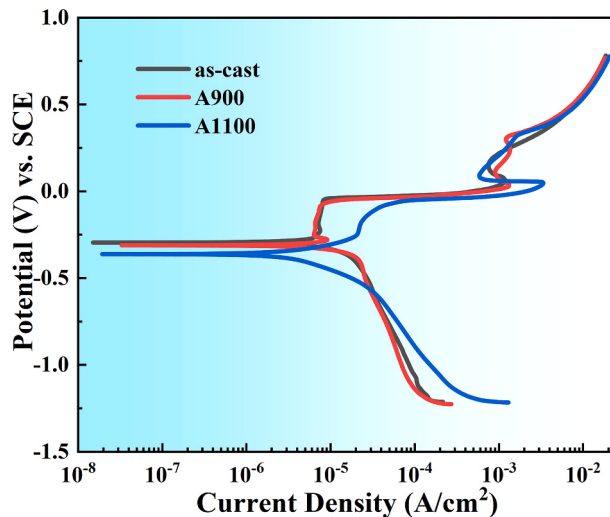


Fig. 10. Potentiodynamic-polarization curves of as-cast and annealed AlCoCuFeTi HEAs in 3.5 wt% NaCl solution.

Table 3
Electrochemical corrosion parameters of as-cast and annealed AlCoCuFeTi HEAs in 3.5 wt% NaCl solution.

Specimens	E_{corr} (mV)	i_{corr} ($\mu\text{A}/\text{cm}^2$)	E_{pit} (mV)	ΔE_p (mV)	CR (mm/year)
as-cast	-295.17	27.35	-46.26	248.91	0.31
A900	-311.25	25.60	-85.22	226.03	0.29
A1100	-362.17	10.03	-149.10	213.07	0.11

4.2. Nanomechanical behaviors

The high hardness of AlCoCuFeTi HEA originates from two aspects: On the one hand, the AlCoCuFeTi alloy mainly comprises L₁ phase, which possesses high hardness and strength at room temperature [32, 54–57]. In addition, as shown in Fig. 6(a), the nano-precipitates in the L₁ phase can act as a strengthening particle to improve its hardness and strength. On the other hand, the formation of Laves phase can also increase the hardness. The variation of nanohardness after annealing is related to the change in volume fractions of different phases. The Cu-enriched FCC phase is a soft phase with low hardness, but the Laves phase is a hard phase. Though the volume fraction of FCC and Laves phases increased in the A900 specimen, the FCC (10.4 %) has a higher volume fraction than the Laves phase (5.4 %), resulting in the decrease of hardness value compared with the as-cast specimen. In contrast, the increase of Laves phase in the A1100 specimen is the main reason for its hardness improvement.

Young's modulus is strongly associated with crystallographic orientations, and the alloys have a higher Young's modulus along the close-packed direction in cubic-crystal materials [58,59]. Fig. 12 displays the inverse pole figures (IPFs) of the L₁ phase for as-cast and annealed AlCoCuFeTi. Based on the TEM result, the L₁ is in an ordered BCC crystal structure. The stronger {111} texture along the Y0 direction would predict a higher Young's modulus in the A900 specimen

Table 4
Molar mixing enthalpy of the constituent binary alloys (kJ/mol).

Element	Al	Co	Cu	Fe	Ti
Al	–	-19	-1	-11	-30
Co		–	+6	-1	-28
Cu			–	+13	-9
Fe				–	-17
Ti					–

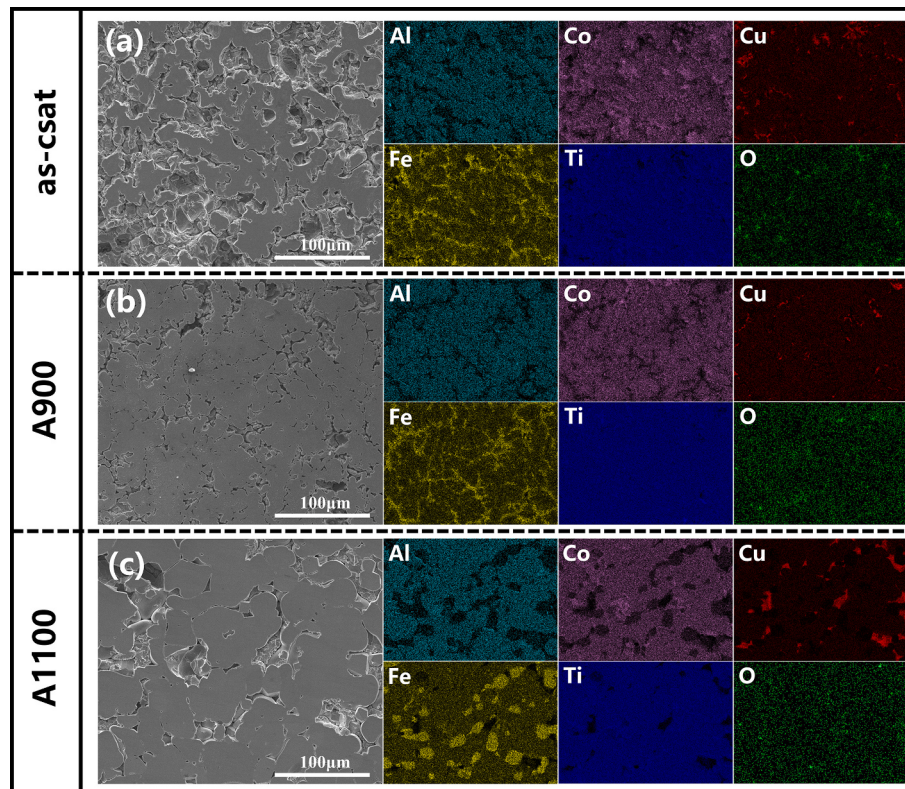


Fig. 11. The corroded surfaces and EDS mapping of as-cast and annealed specimens: (a) as-cast, (b) A900, and (c) A1100.

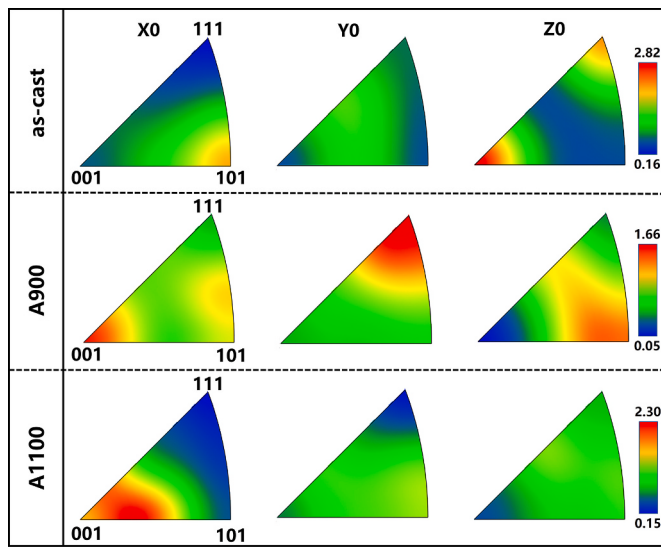


Fig. 12. IPFs of the L₂₁ phase for as-cast and annealed AlCoCuFeTi HEAs.

compared to other specimens since the close-packed direction of BCC crystals is <111>.

4.3. Wear and corrosion behaviors

The sliding of the Si₃N₄ ceramic ball against the HEAs promotes an intense increase in temperature on the worn surface, leading to the formation of a compact oxide layer. The compact oxide layer can act as a protective coating to separate the material and the ceramic ball, thereby improving wear resistance [60,61]. Thus, forming a dense oxide layer on the worn surfaces is the main characteristic contributing to the better wear resistance of AlCoCuFeTi HEAs. Furthermore, the oxide layer can act as a lubricant between the materials and the ceramic ball, thus reducing the COF [62]. When the oxide layer thickness reaches a critical value, the oxide layer will detach from the worn surface owing to internal stress [46]. Hence, the volume loss is mainly due to the oxide layer stripping [63], which can be observed in Fig. 9(a–c). The schematic representation of the wear mechanism in AlCoCuFeTi is illustrated in Fig. 13. Conventional wear theories suggest that alloys with higher hardness possess lower wear rates and better wear resistance. However,

various studies have found that the relationship between wear resistance and hardness does not always hold [15,64,65]. To assess the wear resistance effectively, the ratio of the hardness to the reduced Young's modulus (H/E_r) and yield pressure (H^3/E_r^2) were introduced. The H/E_r value indicates the ability of alloys to resist elastic strain to failure, while the H^3/E_r^2 value represents the resistance to plastic deformation [66]. The higher the H/E_r and H^3/E_r^2 values, the better the wear resistance. As shown in Fig. 14, the A1100 specimen has the highest H/E_r and H^3/E_r^2 values (~0.060 and ~0.052 GPa), which means its best wear resistance. The lowest H/E_r and H^3/E_r^2 values (~0.045 and ~0.024 GPa) were observed in the A900 specimen, implying that it has the worst wear resistance. The H/E_r and H^3/E_r^2 values of as-cast and annealed AlCoCuFeTi alloys are highly consistent with the measured wear rate results.

During galvanic corrosion, L₂₁ and Laves phases are protected as the cathode, while Cu-enriched FCC is seriously corroded as the anode [67]. Furthermore, the galvanic corrosion rate is related to the electrode size, with smaller anodes implying higher current densities, leading to more severe corrosion. Thus, small cathode and large anode are expected in galvanic corrosion [68]. In other words, the larger the area ratio of cathode to anode (A_c/A_a), the faster the corrosion rate is. In the as-cast specimen, the A_c/A_a value is the highest (~14.4), indicating its worst corrosion resistance. After annealing at 900 °C and 1100 °C, the A_c/A_a

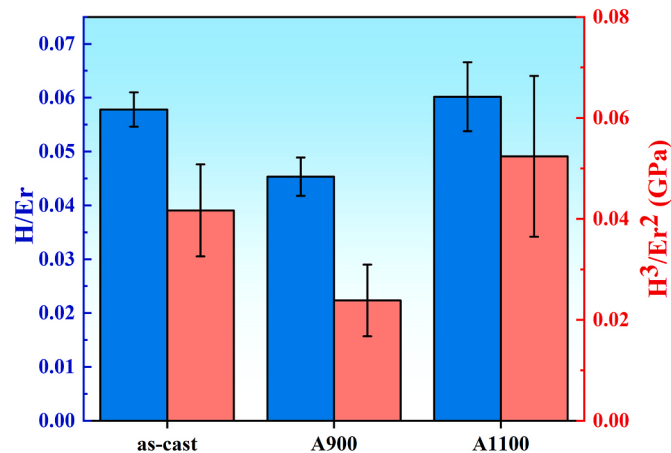


Fig. 14. The elastic strain to failure (H/E_r) and yield pressure (H^3/E_r^2) of as-cast and annealed AlCoCuFeTi HEAs.

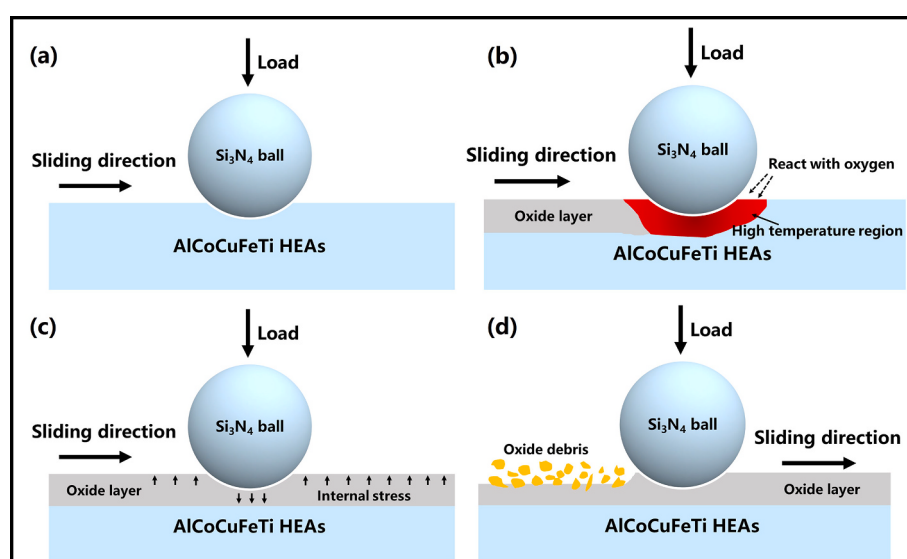


Fig. 13. Schematic representation of wear mechanism during sliding test of AlCoCuFeTi alloy.

values decrease to ~ 8.6 and ~ 6.5 , respectively, which means a better corrosion resistance. The CR values of all specimens also imply that the as-cast specimen has the worst corrosion resistance while the A1100 specimen has the best.

5. Conclusions

In this work, AlCoCuFeTi HEAs with excellent wear resistance and high hardness were successfully fabricated by arc melting. The effect of heat treatment on microstructure, nanomechanical behaviors, tribological properties, and corrosion resistance was investigated in detail. The following conclusions can be drawn:

- (1) The as-cast and annealed AlCoCuFeTi HEAs consist of a Co-enriched L2₁ phase, a Cu-enriched FCC phase, and a Laves phase enriched in Fe and Ti. After annealing at 900 °C and 1100 °C, the L2₁ volume fraction decreased, while the FCC and Laves phase volume fraction increased. The segregation of Cu during solidification was attributed to its high positive mixing enthalpy with other elements.
- (2) Because of L2₁ and Laves phase, the as-cast and annealed AlCo-CuFeTi alloys exhibit high hardness. The A900 specimen shows the highest E_r (256 GPa) compared to the as-cast and A1100 specimens due to its stronger {111} texture. The A1100 specimen possesses the highest hardness owing to its higher Laves phase volume fraction.
- (3) The as-cast and annealed AlCoCuFeTi alloys exhibit outstanding wear resistance compared to typical HEAs. As the annealing temperature increases, the wear rate first improves and then worsens. The A1100 specimen shows higher H/E_r and H³/E_r² values, which accounts for its best wear resistance compared to as-cast and A900 specimens. The shallow scratches and oxide layers on the worn surface indicate mild-oxidational wear is the wear mechanism.
- (4) With the increase of annealing temperature, the corrosion resistance is improved. The segregation of Cu in the ID region leads to galvanic corrosion in AlCoCuFeTi, and the corrosion rate is determined by the A_c/A_a values. The A1100 specimen exhibits the best corrosion resistance due to its lowest A_c/A_a value.

CRediT authorship contribution statement

Xuanjiang Lai: Writing – original draft, Methodology, Investigation, Formal analysis, Data curation. **Yaojia Ren:** Writing – review & editing, Conceptualization. **Qingge Wang:** Writing – review & editing. **Shaohua Xing:** Conceptualization. **Cheng Xu:** Investigation, Data curation. **Jian Hou:** Methodology, Investigation. **Ian Baker:** Writing – review & editing, Methodology. **Hong Wu:** Writing – review & editing, Supervision, Methodology, Funding acquisition.

Declaration of competing interest

The authors declare that they have no known competing financial interests or personal relationships that could have appeared to influence the work reported in this paper.

Data availability

Data will be made available on request.

Acknowledgments

This work was supported by the National Technological Basic Research Program of China, the National Natural Science Foundation of China (Grant No. 52111530193), the Key Research and Development Program of Hunan Province (No. 2022SK2006), the Natural Science

Foundation of Hunan Province for Distinguished Young Scholars (Grant No. 2023JJ10075), and the Fundamental Research Funds for the Central Universities of Central South University (Grant No. 2023ZZTS0490). The authors would also thank Sinoma Institute of Materials Research (Guang Zhou) Co. Ltd. for the assistance with the TEM characterization.

References

- [1] J. Li, Q. Fang, B. Liu, Y. Liu, Y. Liu, Atomic-scale analysis of nanoindentation behavior of high-entropy alloy, *J. Micromech. Mol. Phys.* 1 (1) (2016) 1650001, <https://doi.org/10.1142/S2424913016500016>.
- [2] B. Cantor, Multicomponent high-entropy Cantor alloys, *Prog. Mater. Sci.* 120 (2021) 100754, <https://doi.org/10.1016/j.jpmatsci.2020.100754>.
- [3] P. Sathiyamoorthi, H.S. Kim, High-entropy alloys with heterogeneous microstructure: Processing and mechanical properties, *Prog. Mater. Sci.* 123 (2022) 100709, <https://doi.org/10.1016/j.jpmatsci.2020.100709>.
- [4] W. Li, D. Xie, D. Li, Y. Zhang, Y. Gao, P.K. Liaw, Mechanical behavior of high-entropy alloys, *Prog. Mater. Sci.* 118 (2021) 100777, <https://doi.org/10.1016/j.jpmatsci.2021.100777>.
- [5] D. Wei, L. Wang, Y. Zhang, W. Gong, T. Tsuru, I. Lobzenko, J. Jiang, S. Harjo, T. Kawasaki, J.W. Bae, W. Lu, Z. Lu, Y. Hayasaka, T. Kiguchi, N.L. Okamoto, T. Ichitsubo, H.S. Kim, T. Furuhara, E. Ma, H. Kato, Metalloid substitution elevates simultaneously the strength and ductility of face-centered-cubic high-entropy alloys, *Acta Mater.* 225 (2022) 117571, <https://doi.org/10.1016/j.actamat.2021.117571>.
- [6] Y. Yang, Y. Ren, Y. Tian, K. Li, W. Zhang, Q. Shan, Y. Tian, Q. Huang, H. Wu, Microstructure and properties of FeCoCrNiMoSix high-entropy alloys fabricated by spark plasma sintering, *J. Alloys Compd.* 884 (2021) 161070, <https://doi.org/10.1016/j.jallcom.2021.161070>.
- [7] Y.F. Ye, Q. Wang, J. Lu, C.T. Liu, Y. Yang, High-entropy alloy: challenges and prospects, *Mater. Today* 19 (6) (2016) 349–362, <https://doi.org/10.1016/j.mattod.2015.11.026>.
- [8] A. Sun, W. Zhai, Y. Fu, K. Hu, X. Yang, J. Ke, S. Liu, L. Lv, M. Huang, G. Wang, H. Zhang, Fabrication, high-temperature mechanical behavior, and oxidation resistance of high entropy alloys: a review, *J. Micromech. Mol. Phys.* 8 (02n03) (2023) 99–122, <https://doi.org/10.1142/S2424913023410035>.
- [9] F. Tan, L. Li, J. Li, B. Liu, P.K. Liaw, Q. Fang, Multiscale modelling of irradiation damage behavior in high entropy alloys, *Adv. Powder Mater.* 2 (3) (2023) 100114, <https://doi.org/10.1016/j.apmte.2023.100114>.
- [10] J. Zhang, Z. Zhao, Q. Li, J. Luan, C.-T. Liu, Y. Zhao, T. Yang, Unveiling the unique bifunctionality of L1₂-structured nanoprecipitates in a FeCoNiAlTi-type high-entropy alloy, *Adv. Powder Mater.* 2 (3) (2023) 100113, <https://doi.org/10.1016/j.apmte.2023.100113>.
- [11] X. Duan, T. Han, X. Guan, Y. Wang, H. Su, K. Ming, J. Wang, S. Zheng, Cooperative effect of Cr and Al elements on passivation enhancement of eutectic high-entropy alloy AlCoCrFeNi2.1 with precipitates, *J. Mater. Sci. Technol.* 136 (2023) 97–108, <https://doi.org/10.1016/j.jmst.2022.07.023>.
- [12] J.W. Yeh, S.K. Chen, S.J. Lin, J.Y. Gan, T.S. Chin, T.T. Shun, C.H. Tsau, S.Y. Chang, Nanostructured high-entropy alloys with multiple principal elements: novel alloy Design concepts and outcomes, *Adv. Eng. Mater.* 6 (5) (2004) 299–303, <https://doi.org/10.1002/adem.200300567>.
- [13] B. Cantor, I.T.H. Chang, P. Knight, A.J.B. Vincent, Microstructural development in equiatomic multicomponent alloys, *Mater. Sci. Eng. A* 375–377 (2004) 213–218, <https://doi.org/10.1016/j.msea.2003.10.257>.
- [14] X. Gao, Y. Lu, B. Zhang, N. Liang, G. Wu, G. Sha, J. Liu, Y. Zhao, Microstructural origins of high strength and high ductility in an AlCoCrFeNi2.1 eutectic high-entropy alloy, *Adv. Mater.* 141 (2017) 59–66, <https://doi.org/10.1016/j.actamat.2017.07.041>.
- [15] V. Bhardwaj, Q. Zhou, F. Zhang, W. Han, Y. Du, K. Hua, H. Wang, Effect of Al addition on the microstructure, mechanical and wear properties of TiZrNbHf refractory high entropy alloys, *Tribol. Int.* 160 (2021) 107031, <https://doi.org/10.1016/j.triboint.2021.107031>.
- [16] S.W. Wu, G. Wang, Q. Wang, Y.D. Jia, J. Yi, Q.J. Zhai, J.B. Liu, B.A. Sun, H.J. Chu, J. Shen, P.K. Liaw, C.T. Liu, T.Y. Zhang, Enhancement of strength-ductility trade-off in a high-entropy alloy through a heterogeneous structure, *Acta Mater.* 165 (2019) 444–458, <https://doi.org/10.1016/j.actamat.2018.12.012>.
- [17] D.H. Xiao, P.F. Zhou, W.Q. Wu, H.Y. Diao, M.C. Gao, M. Song, P.K. Liaw, Microstructure, mechanical and corrosion behaviors of AlCoCuFeNi-(Cr,Ti) high entropy alloys, *Mater. Des.* 116 (2017) 438–447, <https://doi.org/10.1016/j.matesdes.2016.12.036>.
- [18] Y. Ren, L. Liang, Q. Shan, A. Cai, J. Du, Q. Huang, S. Liu, X. Yang, Y. Tian, H. Wu, Effect of volumetric energy density on microstructure and tribological properties of FeCoNiCuAl high-entropy alloy produced by laser powder bed fusion, *Virtual Phys. Prototyping* 15 (sup1) (2020) 543–554, <https://doi.org/10.1080/17452759.2020.1848284>.
- [19] Y. Ren, H. Wu, B. Liu, Y. Liu, S. Guo, Z.B. Jiao, I. Baker, A comparative study on microstructure, nanomechanical and corrosion behaviors of AlCoCuFeNi high entropy alloys fabricated by selective laser melting and laser metal deposition, *J. Mater. Sci. Technol.* 131 (2022) 221–230, <https://doi.org/10.1016/j.jmst.2022.05.035>.
- [20] M. Zhang, X. Zhou, D. Wang, W. Zhu, J. Li, Y.F. Zhao, AlCoCuFeNi high-entropy alloy with tailored microstructure and outstanding compressive properties fabricated via selective laser melting with heat treatment, *Mater. Sci. Eng. A* 743 (2019) 773–784, <https://doi.org/10.1016/j.msea.2018.11.118>.

- [21] Y.X. Zhuang, H.D. Xue, Z.Y. Chen, Z.Y. Hu, J.C. He, Effect of annealing treatment on microstructures and mechanical properties of FeCoNiCuAl high entropy alloys, *Mater. Sci. Eng. A* 572 (2013) 30–35, <https://doi.org/10.1016/j.msea.2013.01.081>.
- [22] Z. Lyu, C. Lee, S.-Y. Wang, X. Fan, J.-W. Yeh, P.K. Liaw, Effects of constituent elements and fabrication methods on mechanical behavior of high-entropy alloys: a review, *Metall. Mater. Trans. A* 50 (1) (2019) 1–28, <https://doi.org/10.1007/s11661-018-4970-z>.
- [23] Y. Li, Y. Shi, Phase assemblage and properties of laser cladded Ti_xCrFeCoNiCu high-entropy alloy coating on aluminum, *Mater. Res. Express* 7 (3) (2020) 036519, <https://doi.org/10.1088/2053-1591/ab7d0c>.
- [24] Y. Zhao, K.B. Lau, W.H. Teh, J.J. Lee, F. Wei, M. Lin, P. Wang, C.C. Tan, U. Ramamurti, Compositonally graded CoCrFeNiTi_x high-entropy alloys manufactured by laser powder bed fusion: a combinatorial assessment, *J. Alloys Compd.* 883 (2021) 160825, <https://doi.org/10.1016/j.jallcom.2021.160825>.
- [25] X.-c. Ye, T. Wang, Z.-y. Xu, C. Liu, H.-h. Wu, G.-w. Zhao, D. Fang, Effect of Ti content on microstructure and mechanical properties of Cu₂FeNi high-entropy alloys, *Int. J. Miner. Metall. Mater.* 27 (10) (2020) 1326–1331, <https://doi.org/10.1007/s12613-020-2024-1>.
- [26] M. Wu, R.C. Setiawan, D.Y. Li, Benefits of passive element Ti to the resistance of AlCrFeCoNi high-entropy alloy to corrosion and corrosive wear, *Wear* 492–493 (2022) 204231, <https://doi.org/10.1016/j.wear.2021.204231>.
- [27] Y. Zhao, M. Wang, H. Cui, Y. Zhao, X. Song, Y. Zeng, X. Gao, F. Lu, C. Wang, Q. Song, Effects of Ti-to-Al ratios on the phases, microstructures, mechanical properties, and corrosion resistance of Al₂-xCoCrFeNiTi_x high-entropy alloys, *J. Alloys Compd.* 805 (2019) 585–596, <https://doi.org/10.1016/j.jallcom.2019.07.100>.
- [28] X. Gu, Y. Zhuang, D. Huang, Corrosion behaviors related to the microstructural evolutions of as-cast Al_{0.3}CoCrFeNi high entropy alloy with addition of Si and Ti elements, *Intermetallics* 147 (2022) 107600, <https://doi.org/10.1016/j.intermet.2022.107600>.
- [29] L. Jiang, H. Jiang, Y. Lu, T. Wang, Z. Cao, T. Li, Mechanical properties improvement of AlCrFeNi₂Ti_{0.5} high entropy alloy through annealing design and its relationship with its particle-reinforced microstructures, *J. Mater. Sci. Technol.* 31 (4) (2015) 397–402, <https://doi.org/10.1016/j.jmst.2014.09.011>.
- [30] G. Laplanche, O. Horst, F. Otto, G. Eggeler, E.P. George, Microstructural evolution of a CoCrFeMnNi high-entropy alloy after swaging and annealing, *J. Alloys Compd.* 647 (2015) 548–557, <https://doi.org/10.1016/j.jallcom.2015.05.129>.
- [31] Q.H. Tang, Y. Huang, Y.Y. Huang, X.Z. Liao, T.G. Langdon, P.Q. Dai, Hardening of an Al_{0.3}CoCrFeNi high entropy alloy via high-pressure torsion and thermal annealing, *Mater. Lett.* 151 (2015) 126–129, <https://doi.org/10.1016/j.matlet.2015.03.066>.
- [32] W. Guo, J. Li, M. Qi, Y. Xu, H.R. Ezatpour, Effects of heat treatment on the microstructure, mechanical properties and corrosion resistance of AlCoCrFeNiTi_{0.5} high-entropy alloy, *J. Alloys Compd.* 884 (2021) 161026, <https://doi.org/10.1016/j.jallcom.2021.161026>.
- [33] J.-T. Liang, K.-C. Cheng, S.-H. Chen, Effect of heat treatment on the phase evolution and mechanical properties of atomized AlCoCrFeNi high-entropy alloy powders, *J. Alloys Compd.* 803 (2019) 484–490, <https://doi.org/10.1016/j.jallcom.2019.06.301>.
- [34] S. Minghong, Z. Li, Z. Junwei, L. Na, L. Taizeng, W. Ning, Effects of annealing on the microstructure and wear resistance of AlCoCrFeNiTi_{0.5} high-entropy alloy coating prepared by laser cladding, *Rare Met. Mater. Eng.* 46 (5) (2017) 1237–1240, [https://doi.org/10.1016/S1875-5372\(17\)30143-1](https://doi.org/10.1016/S1875-5372(17)30143-1).
- [35] D. Kong, J. Guo, R. Liu, X. Zhang, Y. Song, Z. Li, F. Guo, X. Xing, Y. Xu, W. Wang, Effect of remelting and annealing on the wear resistance of AlCoCrFeNiTi_{0.5} high entropy alloys, *Intermetallics* 114 (2019) 106560, <https://doi.org/10.1016/j.intermet.2019.106560>.
- [36] S. Wang, Y. Zhao, X. Xu, P. Cheng, H. Hou, Evolution of mechanical properties and corrosion resistance of Al_{0.6}CoFeNiCr_{0.4} high-entropy alloys at different heat treatment temperature, *Mater. Chem. Phys.* 244 (2020) 122700, <https://doi.org/10.1016/j.matchemphys.2020.122700>.
- [37] Y. Shi, L. Collins, R. Feng, C. Zhang, N. Balke, P.K. Liaw, B. Yang, Homogenization of Al_xCoCrFeNi high-entropy alloys with improved corrosion resistance, *Corros. Sci.* 133 (2018) 120–131, <https://doi.org/10.1016/j.corsci.2018.01.030>.
- [38] X.F. Wang, Y. Zhang, Y. Qiao, G.L. Chen, Novel microstructure and properties of multicomponent CoCrFeNiTi_x alloys, *Intermetallics* 15 (3) (2007) 357–362, <https://doi.org/10.1016/j.intermet.2006.08.005>.
- [39] G. Qin, Z. Li, R. Chen, H. Zheng, C. Fan, L. Wang, Y. Su, H. Ding, J. Guo, H. Fu, CoCrFeMnNi high-entropy alloys reinforced with Laves phase by adding Nb and Ti elements, *J. Mater. Res.* 34 (6) (2019) 1011–1020, <https://doi.org/10.1557/jmr.2018.468>.
- [40] S. Wan, X. Cui, S. Wang, Y. Zhao, G. Jin, W. Su, Y. Yang, J. Ma, J. Li, A novel laser-cladded AlCuTiVCr/Cu-Al functionally graded coating with excellent corrosion resistance on Mg-Al alloy, *Mater. Lett.* 350 (2023) 134944, <https://doi.org/10.1016/j.matlet.2023.134944>.
- [41] C.F. Tey, X. Tan, S.L. Sing, W.Y. Yeong, Additive manufacturing of multiple materials by selective laser melting: Ti-alloy to stainless steel via a Cu-alloy interlayer, *Addit. Manuf.* 31 (2020) 100970, <https://doi.org/10.1016/j.addma.2019.100970>.
- [42] T. Zhu, H. Wu, R. Zhou, N. Zhang, Y. Yin, L. Liang, Y. Liu, J. Li, Q. Shan, Q. Li, W. Huang, Microstructures and tribological properties of TiC reinforced FeCoNiCuAl high-entropy alloy at normal and elevated temperature, *Metals* 10 (3) (2020), <https://doi.org/10.3390/met10030387>.
- [43] Y. Wang, Y. Yang, H. Yang, M. Zhang, J. Qiao, Effect of nitriding on the tribological properties of Al_{11.3}Co₂Cu₂Ni₂ high-entropy alloy, *J. Alloys Compd.* 725 (2017) 365–372, <https://doi.org/10.1016/j.jallcom.2017.07.132>.
- [44] J.-M. Wu, S.-J. Lin, J.-W. Yeh, S.-K. Chen, Y.-S. Huang, H.-C. Chen, Adhesive wear behavior of Al_xCoCrCuFeNi high-entropy alloys as a function of aluminum content, *Wear* 261 (5) (2006) 513–519, <https://doi.org/10.1016/j.wear.2005.12.008>.
- [45] P. Shi, Y. Yu, N. Xiong, M. Liu, Z. Qiao, G. Yi, Q. Yao, G. Zhao, E. Xie, Q. Wang, Microstructure and tribological behavior of a novel atmospheric plasma sprayed AlCoCrFeNi high entropy alloy matrix self-lubricating composite coatings, *Tribol. Int.* 151 (2020) 106470, <https://doi.org/10.1016/j.triboint.2020.106470>.
- [46] A. Zhang, J. Han, B. Su, P. Li, J. Meng, Microstructure, mechanical properties and tribological performance of CoCrFeNi high entropy alloy matrix self-lubricating composite, *Mater. Des.* 114 (2017) 253–263, <https://doi.org/10.1016/j.matdes.2016.11.072>.
- [47] T.F. Quinn, Review of oxidational wear: Part I: the origins of oxidational wear, *Tribol. Int.* 16 (5) (1983) 257–271, [https://doi.org/10.1016/0301-679X\(83\)90085-5](https://doi.org/10.1016/0301-679X(83)90085-5).
- [48] F.H. Stott, The role of oxidation in the wear of alloys, *Tribol. Int.* 31 (1) (1998) 61–71, [https://doi.org/10.1016/S0301-679X\(98\)00008-5](https://doi.org/10.1016/S0301-679X(98)00008-5).
- [49] Y. Yu, F. He, Z. Qiao, Z. Wang, W. Liu, J. Yang, Effects of temperature and microstructure on the tribological properties of CoCrFeNiNb_x eutectic high entropy alloys, *J. Alloys Compd.* 775 (2019) 1376–1385, <https://doi.org/10.1016/j.jallcom.2018.10.138>.
- [50] L.M. Du, L.W. Lan, S. Zhu, H.J. Yang, X.H. Shi, P.K. Liaw, J.W. Qiao, Effects of temperature on the tribological behavior of Al_{0.25}CoCrFeNi high-entropy alloy, *J. Mater. Sci. Technol.* 35 (5) (2019) 917–925, <https://doi.org/10.1016/j.jmst.2018.11.023>.
- [51] M. Pole, M. Sadeghilaridjani, J. Shittu, A. Ayyagari, S. Mukherjee, High temperature wear behavior of refractory high entropy alloys based on 4-5 elemental palette, *J. Alloys Compd.* 843 (2020) 156004, <https://doi.org/10.1016/j.jallcom.2020.156004>.
- [52] A. Verma, P. Tarate, A.C. Abhyankar, M.R. Mohapse, D.S. Gowtam, V.P. Deshmukh, T. Shanmugasundaram, High temperature wear in CoCrFeNiCu high entropy alloys: the role of Cu, *Scr. Mater.* 161 (2019) 28–31, <https://doi.org/10.1016/j.scriptamat.2018.10.007>.
- [53] L. Liu, Y. Zhang, J. Han, X. Wang, W. Jiang, C.-T. Liu, Z. Zhang, P.K. Liaw, Nanoprecipitate-Strengthened high-entropy alloys, *Adv. Sci.* 8 (23) (2021) 2100870, <https://doi.org/10.1002/advs.202100870>.
- [54] X. Zeng, Z. Liu, G. Wu, X. Tong, Y. Xiong, X. Cheng, X. Wang, T. Yamaguchi, Microstructure and high-temperature properties of laser cladded AlCoCrFeNiTi_{0.5} high-entropy coating on Ti 6Al-4V alloy, *Surf. Coat. Technol.* 418 (2021) 127243, <https://doi.org/10.1016/j.surcoat.2021.127243>.
- [55] Y. Qi, Y. Wu, T. Cao, L. He, F. Jiang, J. Sun, L21-strengthened face-centered cubic high-entropy alloy with high strength and ductility, *Mater. Sci. Eng. A* 797 (2020) 140056, <https://doi.org/10.1016/j.msea.2020.140056>.
- [56] Y. Xiao, X. Peng, T. Fu, L21-strengthened body-centered-cubic high-entropy alloy with excellent mechanical properties, *Intermetallics* 145 (2022) 107539, <https://doi.org/10.1016/j.intermet.2022.107539>.
- [57] W.C. Kim, M.Y. Na, H.J. Kwon, Y.S. Na, J.W. Won, H.J. Chang, K.R. Lim, Designing L21-strengthened Al-Cr-Fe-Ni-Ti complex concentrated alloys for high temperature applications, *Acta Mater.* 211 (2021) 116890, <https://doi.org/10.1016/j.actamat.2021.116890>.
- [58] P. Wang, M. Todai, T. Nakano, Beta titanium single crystal with bone-like elastic modulus and large crystallographic elastic anisotropy, *J. Alloys Compd.* 782 (2019) 667–671, <https://doi.org/10.1016/j.jallcom.2018.12.236>.
- [59] Y.X. Ye, B.L. Musico, Z.Z. Lu, L.B. Xu, Z.F. Lei, V. Keppens, H.X. Xu, T.G. Nieh, Evaluating elastic properties of a body-centered cubic NbHfZrTi high-entropy alloy – a direct comparison between experiments and ab initio calculations, *Intermetallics* 109 (2019) 167–173, <https://doi.org/10.1016/j.intermet.2019.04.003>.
- [60] M.-H. Chuang, M.-H. Tsai, W.-R. Wang, S.-J. Lin, J.-W. Yeh, Microstructure and wear behavior of AlxCu_{1.5}CrFeNi_{1.5}Ti_y high-entropy alloys, *Acta Mater.* 59 (16) (2011) 6308–6317, <https://doi.org/10.1016/j.actamat.2011.06.041>.
- [61] S.C. Lim, The relevance of wear-mechanism maps to mild-oxidational wear, *Tribol. Int.* 35 (11) (2002) 717–723, [https://doi.org/10.1016/S0301-679X\(02\)00033-6](https://doi.org/10.1016/S0301-679X(02)00033-6).
- [62] Z. Guo, A. Zhang, J. Han, J. Meng, Microstructure, mechanical and tribological properties of CoCrFeNiMn high entropy alloy matrix composites with addition of Cr₃C₂, *Tribol. Int.* 151 (2020) 106436, <https://doi.org/10.1016/j.triboint.2020.106436>.
- [63] T.F. Quinn, Oxidational wear, *Wear* 18 (5) (1971) 413–419, [https://doi.org/10.1016/0043-1648\(71\)90005-6](https://doi.org/10.1016/0043-1648(71)90005-6).
- [64] J. Joseph, N. Haghdi, K. Shamlaye, P. Hodgson, M. Barnett, D. Fabijanic, The sliding wear behaviour of CoCrFeMnNi and AlxCuCrFeNi high entropy alloys at elevated temperatures, *Wear* 428–429 (2019) 32–44, <https://doi.org/10.1016/j.wear.2019.03.002>.
- [65] B. Narayanaswamy, P. Hodgson, H. Beladi, Comparisons of the two-body abrasive wear behaviour of four different ferrous microstructures with similar hardness levels, *Wear* 350–351 (2016) 155–165, <https://doi.org/10.1016/j.wear.2016.01.013>.
- [66] A.M. Okoro, R. Machaka, S.S. Lephuthing, S.R. Oke, M.A. Awotunde, P. A. Olubambi, Nanoindentation studies of the mechanical behaviours of spark plasma sintered multiwall carbon nanotubes reinforced Ti₆Al₄V nanocomposites,

- Mater. Sci. Eng. A 765 (2019) 138320, <https://doi.org/10.1016/j.msea.2019.138320>.
- [67] Y. Shi, B. Yang, P.K. Liaw, Corrosion-resistant high-entropy alloys: a review, Metals 7 (2) (2017), <https://doi.org/10.3390/met7020043>.
- [68] F. Mansfeld, Area relationships in galvanic corrosion, Corrosion 27 (10) (2013) 436–442, <https://doi.org/10.5006/0010-9312-27.10.436>.